A&A 581, A41 (2015)
DOI: 10.1051/0004-6361/201526061

Astronomy & Astrophysics

OmegaWINGS: OmegaCAM-VST observations of WINGS galaxy clusters⋆,⋆⋆

M. Gullieuszik[1], B. Poggianti[1], G. Fasano[1], S. Zaggia[1], A. Paccagnella[1,2], A. Moretti[1,2], D. Bettoni[1], M. D'Onofrio[1], W. J. Couch[3], B. Vulcani[4], J. Fritz[5,6], A. Omizzolo[1,7], A. Baruffolo[1], P. Schipani[8], M. Capaccioli[9], and J. Varela[10]

[1] INAF–Osservatorio astronomico di Padova, Vicolo dell'Osservatorio 5, 35122 Padova, Italy
e-mail: marco.gullieuszik@oapd.inaf.it
[2] Dipartimento di Fisica e Astronomia, Università degli Studi di Padova, Vicolo dell'Osservatorio 3, 35122 Padova, Italy
[3] Australian Astronomical Observatory, PO Box 915, North Ryde, NSW 1670, Australia
[4] Kavli Institute for the Physics and Mathematics of the Universe (WPI), Todai Institutes for Advanced Study, the University of Tokyo, 277-8582 Kashiwa, Japan
[5] Sterrenkundig Observatorium Vakgroep Fysica en Sterrenkunde Universiteit Gent, Krijgslaan 281, S9 9000 Gent, Belgium
[6] Centro de Radioastronomía y Astrofisíca, UNAM, Campus Morelia, A.P. 3-72, CP 58089 Michoacán, Mexico
[7] Specola Vaticana, 00120 Cittá Del Vaticana, Vatican City State
[8] INAF–Osservatorio astronomico di Capodimonte, Salita Moiariello 16, 80131 Napoli, Italy
[9] Dipartimento di Fisica, Università Federico II, via Cinthia, 80126 Napoli, Italy
[10] Centro de Estudios de Fisica del Cosmos de Aragon, Plaza San Juan, 1, 44001 Teruel, Spain

Received 9 March 2015 / Accepted 19 May 2015

ABSTRACT

Context. Wide-field observations targeting galaxy clusters at low redshift are complementary to field surveys and provide the local benchmark for detailed studies of the most massive haloes in the local Universe. The Wide-field Nearby Galaxy-cluster Survey (WINGS) is a wide-field multi-wavelength survey of X-ray selected clusters at $z = 0.04$–0.07. The original $34' \times 34'$ WINGS field of view has now been extended to cover a 1 deg^2 field with both photometry and spectroscopy.
Aims. We present the Johnson *B*- and *V*-band OmegaCAM at the VST observations of 46 WINGS clusters together with the data reduction, data quality, and Sextractor photometric catalogues.
Methods. The data reduction was carried out with a modified version of the ESO-MVM (also known as ALAMBIC) reduction package, adding a cross-talk correction, the gain harmonisation, and a control procedure for problematic CCDs. The stray-light component was corrected for by employing our own observations of populated stellar fields.
Results. With a median seeing of $1''$ in both bands, our 25-min exposures in each band typically reach the 50% completeness level at $V = 23.1$ mag. The quality of the astrometric and photometric accuracy has been verified by comparison with the 2MASS and SDSS astrometry, and SDSS and previous WINGS imaging. Star-to-galaxy separation and sky-subtraction procedure were tested comparing them with previous WINGS data.
Conclusions. The Sextractor photometric catalogues are publicly available at the CDS and will be included in the next release of the WINGS database on the Virtual Observatory together with the OmegaCAM reduced images. These data form the basis for a large ongoing spectroscopic campaign with AAOmega at the AAT and are being employed for a variety of studies.

Key words. methods: observational – catalogs – galaxies: clusters: general – galaxies: photometry – galaxies: fundamental parameters

1. Introduction

Galaxy clusters, the most massive collapsed structures in the Universe, play an important role for both cosmology and galaxy evolution studies. They are the tail of a continuum distribution of halo masses and are the most extreme environments where galaxy formation has proceeded at an accelerated rate compared to the rest of the Universe. Clusters have been a testbed for studies of galaxy formation and evolution, uncovering trends that several years later have also been found in the field (Butcher & Oemler 1978; Couch & Sharples 1987; Dressler et al. 1997). They are a repository for galaxies that have been shaped in lower halo-mass environments (Lewis et al. 2002; Poggianti et al. 2006; Balogh et al. 2009; Wilman et al. 2009), but also the sites where essentially all environmental effects are thought to take place, from strangulation to ram pressure stripping, and even mergers (Gunn & Gott 1972; Larson et al. 1980; Balogh et al. 2000; Boselli & Gavazzi 2006; De Lucia et al. 2010). As peaks in the matter distribution, they host those galaxies that have formed first and in the most extreme primordial conditions, and at the same time, hierarchical growth is most evident in them, for instance, in the brightest cluster galaxies. There is no better place than rich clusters in the low-z Universe to find and study the descendants of the most massive galaxies observed at high-z (Poggianti et al. 2013).

The WIde-field Nearby Galaxy-cluster Survey (WINGS) is a wide-field and multiwavelength survey of 76 galaxy clusters in the local Universe (Fasano et al. 2006). The sample consists of all clusters at $0.04 < z < 0.07$ in both hemispheres at Galactic latitude $|b| \geq 20$ selected from the ROSAT X-ray-Brightest

⋆ Based on observations made with VST at ESO Paranal Observatory under program ID 88.A-4005, 089.A-0023, 090.A-0074, 091.A-0059, and 093.A-0041.
⋆⋆ The photometric catalogue is only available at the CDS via anonymous ftp to cdsarc.u-strasbg.fr (130.79.128.5) or via http://cdsarc.u-strasbg.fr/viz-bin/qcat?J/A+A/581/A41

Abell-type Cluster Sample, the Brightest Cluster Sample, and its extension (Ebeling et al. 1996, 1998, 2000).

The original WINGS survey is based on B and V imaging for the 76 clusters over a $34' \times 34'$ field of view (FOV) taken with the Wide Field Cameras on the INT and the 2.2m MPG/ESO telescopes (Varela et al. 2009). J- and K-band Wide Field Camera imaging at UKIRT (Valentinuzzi et al. 2009) and U-band imaging with the INT, LBT, and BOK telescopes (Omizzolo et al. 2014) were secured for a subset of clusters. Spectroscopy was obtained over the $34' \times 34'$ FOV with 2dF-AAT (~4000 usable spectra) and WYFFOS-WHT (~2500 spectra) (Cava et al. 2009). These data allowed us to derive galaxy morphologies (Fasano et al. 2012), surface photometry and sizes (D'Onofrio et al. 2014), stellar masses, star formation histories, and spectral types (Fritz et al. 2011, 2014; Vulcani et al. 2011), as well as to characterise the cluster substructure and dynamics (Ramella et al. 2007; Cava et al., in prep.). We also conducted a number of studies on galaxy properties and evolution (a full publication list can be found at the WINGS website[1]). The WINGS data and data products are publicly available through the Virtual Observatory (VO), as explained in Moretti et al. (2014).

The WINGS optical images, together with the photometry and source classification, were used to calibrate the photometry presented in this paper and for other purposes, as described in the following sections.

The WINGS dataset is unique, as none of the other low-z surveys investigate a large sample of clusters and cluster galaxies in such detail. GAMA offers an exquisite sampling down to low-mass haloes, but it lacks a large number of massive clusters at redshifts that would be similar to those of WINGS (Robotham et al. 2011). The SDSS (York et al. 2000) provides large cluster catalogues, but has a much lower imaging quality (for seeing, depth, and pixel scale, see below), and is 1.5 mag shallower than WINGS spectroscopy, yielding a smaller dynamic range of galaxy magnitudes and masses at the WINGS redshifts.

The main limitation of the original WINGS data is that they only cover the cluster cores: the maximum clustercentric distance reached in (almost) all clusters by the INT+2.2m imaging is only 0.6 times the virial radius. Crucially, the coverage out to at least the virial radius and into the outer regions is missing. This would be of primary importance, as it would link clusters with the surrounding populations and the field.

Clusters accrete individual galaxies and larger subclumps from their outskirts. The outer regions of clusters are the transition regions between the cores, with their dense and hot intracluster medium, and the filaments (and/or groups) feeding the cluster, at the point where galaxies are subject to a dramatic change of environment. Indeed, observations have proved that the cluster outskirts are essential for understanding galaxy transformations (Lewis et al. 2002; Pimbblet et al. 2002; Treu et al. 2003; Moran et al. 2007). Moreover, the projected clustercentric radius of galaxies statistically retains memory of the epoch when the galaxy first became part of a massive structure and became a satellite (Smith et al. 2012; De Lucia et al. 2012). Cosmological hydrodynamical simulations predict a depletion of both hot and cold gas and a decline in the star-forming fraction of galaxies as far out as five cluster virial radii (Bahé et al. 2013). With the exception of a few single clusters and superclusters (e.g., Merluzzi et al. 2010, 2015; Mahajan et al. 2011; Smith et al. 2012; Haines et al. 2011), this very important transition region between clusters and the surrounding field remains largely unexplored.

[1] http://web.oapd.inaf.it/wings

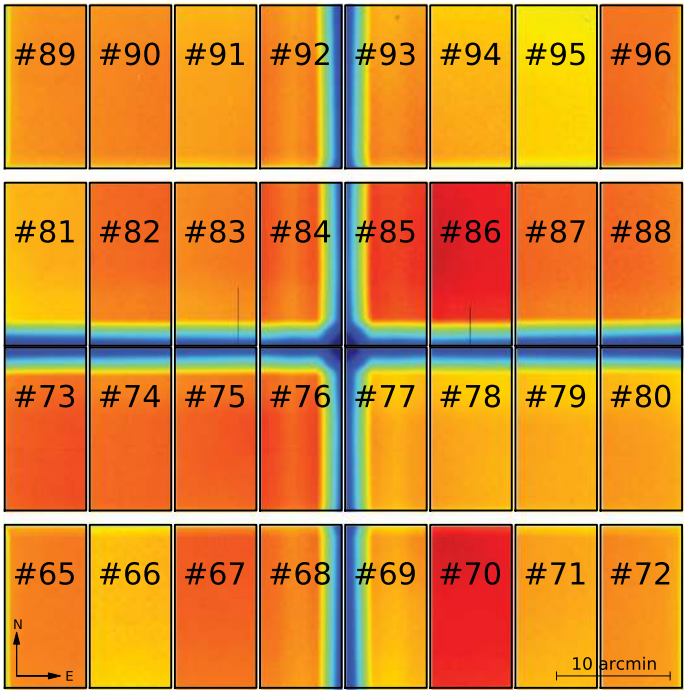

Fig. 1. Layout of the OmegaCAM CCD mosaic. The labels indicate the ESO ID of each chip. The image is a V-band raw flat-field image.

With the aim to cover the virial region and extend out into the infall region, we have obtained GTO OmegaCAM/VST imaging in the u, B, and V bands over 1×1 deg^2 for 45 fields covering 46 WINGS clusters. A large spectroscopic follow-up campaign targeting all 46 clusters is ongoing with AAOmega-AAT (Moretti et al., in prep.). This imaging+spectroscopic dataset is from now on named OmegaWINGS.

This paper presents the OmegaCAM-VST B and V imaging, the observations (Sect. 2), data reduction (Sect. 3), the release of photometric catalogues (Sect. 4) and data quality (Sect. 5). The u-band campaign is still ongoing and will be presented in a subsequent paper.

In the following, we use $H_0 = 70\,\mathrm{km\,s^{-1}\,Mpc^{-1}}$, $\Omega_\mathrm{m} = 0.3$, $\Omega_\mathrm{lambda} = 0.7$.

2. Observations

The VLT Survey Telescope (VST, Capaccioli & Schipani 2011) is a 2.6 m wide field optical telescope placed at Cerro Paranal, Chile. The telescope is equipped with OmegaCAM (Kuijken 2011), a camera that samples the 1 deg^2 VST unvignetted FOV with a mosaic of 32 4k× 2k CCDs at $0\farcs21$/pix. The layout of the OmegaCAM mosaic is shown in Fig. 1; the ESO identification name is superimposed to each CCD.

OmegaWINGS target clusters were randomly selected from the 57 WINGS clusters that can be observed from VST ($\delta < 20°$). We obtained service-mode B- and V-band imaging for 46 of them with 45 OmegaCAM pointings. Two WINGS clusters, A3528a and A3528b, were observed with a single VST pointing; hereafter this is referred to as A3528. The position of the target clusters observed by the OmegaWINGS survey are shown in Fig. 2. The choice of BV filters was taken for consistency with the original WINGS survey, despite the problems related with the segmentation of the OmegaCAM Johnson filters that are discussed at the end of this section.

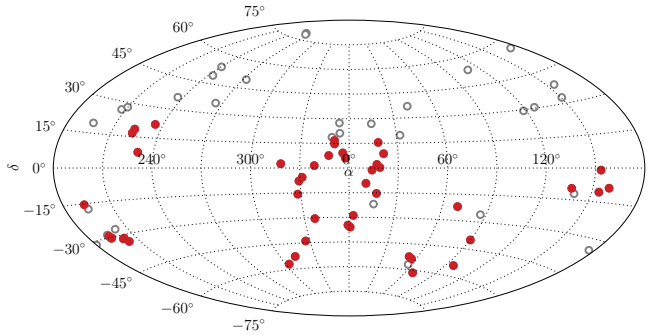

Fig. 2. OmegaWINGS target clusters are shown as filled circles, all WINGS clusters are shown as open circles.

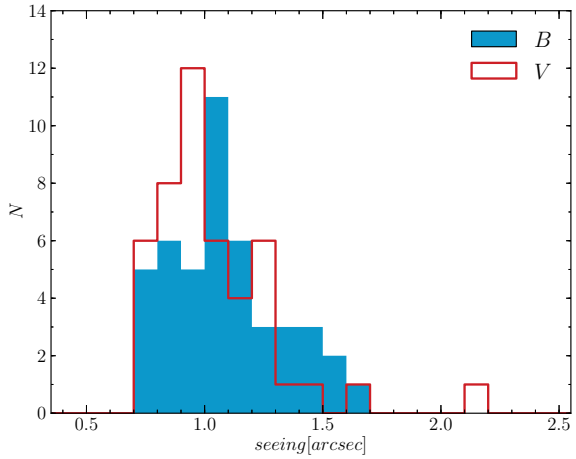

Fig. 3. Mean seeing measured on stacked OmegaWINGS *B*- and *V*-band images.

Observations started in October 2011 and were concluded in September 2013. The first observations were carried out during ESO period P88 with the OmegaCAM *STARE-mode*, splitting the total exposure time into 3 × 480 s observations with no offsets. We adopted this observing mode to obtain a constant signal-to-noise ratio (S/N) across the FOV, as in the original WINGS survey. Starting from period P89, we optimised our observing strategy, taking 5 × 300 s exposures in *DITHER-mode*, with 25″ and 85″ offsets in horizontal and vertical direction, respectively. This observing strategy offers two major advantages: it allows dithering out the gaps between the CCDs and estimating the contribution of the background light (see next section for details). The log of our observations is summarised in Table 1.

On average, seeing was better during *V*-band observations than during *B*-band ones. We measured the seeing in each OmegaWINGS image as the mean value of the FWHM of the stellar profiles. The values are listed in Table 1 and shown in Fig. 3. The seeing is lower than 1.″3 in 80% of the *B*-band images and lower than 1.″2 in 80% of the *V*-band images. The median seeing values are 1.″0 in both *B* and *V* band.

Since OmegaCAM *B* and *V* filters are segmented and composed of four quadrants, the interface of the quadrants casts a slight shadow in the form of a cross onto the image plane. This central vignetting cross is ∼310″ wide in both directions. Figure 1 shows a raw flat-field image in the *V* band, where the vignetting is clearly visible. To remove it from the final stacked images, the OmegaCAM User Manual[2] suggests a dithering pattern with steps 310″ wide in both *X* and *Y* direction. Steps this wide would reduce the FOV covered by five exposures. Considering that the central region of each target cluster is covered by WINGS data, we decided to use smaller dithering steps. However, in this way, the vignetting cross cannot be entirely removed, and our final images have a vertical stripe ∼3′ wide that is strongly affected by vignetting and that was therefore masked out. The horizontal component of the vignetting cross instead was perfectly removed.

[2] http://www.eso.org/sci/facilities/paranal/instruments/omegacam/doc.html

Table 1. Observation log.

Cluster	DATEOBS$_B$	σ_B	DATEOBS$_V$	σ_V	src
A85	2013-09-03	0.″97	2013-08-03	1.″00	SDSS
A119	2011-12-17	1.″03	2011-10-23	0.″74	SDSS
A147	2013-07-15	0.″78	2013-08-05	0.″83	SDSS
A151	2012-11-17	0.″85	2012-11-04	0.″75	2MASS
A160	2011-10-21	0.″79	2011-10-21	0.″99	SDSS
A168	2013-07-18	1.″17	2013-08-03	1.″23	SDSS
A193	2011-10-21	0.″78	2011-10-21	1.″01	SDSS
A500	2011-11-28	1.″26	2011-12-02	1.″28	2MASS
A754	2011-11-30	0.″76	2011-11-22	0.″95	2MASS
A957x	2012-03-26	1.″05	2011-11-23	1.″02	SDSS
A970	2011-12-23	1.″64	2011-11-24	1.″25	2MASS
A1069	2013-04-13	1.″31	2013-05-07	0.″87	2MASS
A1631a	2013-03-22	1.″16	2013-02-10	0.″98	2MASS
A1983	2012-05-18	1.″05	2012-03-31	1.″23	SDSS
A1991	2013-04-15	0.″86	2013-04-14	0.″84	SDSS
A2107	2013-04-08	1.″03	2013-04-10	1.″01	SDSS
A2382	2012-07-20	1.″03	2012-06-26	2.″12	2MASS
A2399	2012-06-16	0.″84	2012-05-29	1.″24	SDSS
A2415	2012-07-26	1.″49	2012-07-22	0.″82	SDSS
A2457	2012-06-16	1.″08	2012-07-15	1.″13	SDSS
A2589	2013-07-16	1.″22	2013-07-13	0.″96	SDSS
A2593	2012-10-08	1.″41	2012-10-08	1.″01	SDSS
A2657	2013-07-17	0.″78	2013-07-11	0.″77	SDSS
A2665	2013-07-12	0.″96	2013-07-12	0.″96	SDSS
A2717	2013-08-01	1.″57	2013-06-11	1.″22	2MASS
A2734	2013-06-20	1.″13	2013-07-07	1.″06	2MASS
A3128	2011-12-20	1.″03	2011-12-18	0.″77	2MASS
A3158	2011-12-18	0.″95	2011-12-20	0.″93	2MASS
A3266	2012-10-15	1.″53	2012-10-15	1.″10	2MASS
A3376	2013-01-04	1.″01	2012-11-17	1.″32	2MASS
A3395	2013-03-05	0.″89	2013-03-02	1.″11	2MASS
A3528	2013-06-02	1.″43	2013-06-05	1.″11	2MASS
A3530	2013-06-03	0.″95	2013-06-06	0.″86	2MASS
A3532	2013-06-03	0.″91	2013-06-07	0.″77	2MASS
A3556	2012-06-17	1.″21	2012-05-24	1.″44	2MASS
A3558	2013-06-11	0.″85	2013-06-28	0.″76	2MASS
A3560	2012-06-18	0.″89	2012-05-24	1.″68	2MASS
A3667	2013-04-13	1.″38	2013-05-14	0.″95	2MASS
A3716	2013-05-20	1.″13	2013-05-20	0.″93	2MASS
A3809	2012-07-22	1.″12	2012-04-18	0.″99	2MASS
A3880	2013-06-11	1.″31	2013-06-20	0.″92	2MASS
A4059	2013-08-04	1.″05	2013-07-03	0.″91	2MASS
IIZW108	2013-06-06	1.″04	2013-06-06	0.″86	SDSS
MKW3s	2012-04-20	1.″14	2012-04-19	0.″83	SDSS
Z8852	2012-11-10	1.″02	2012-10-12	0.″83	SDSS

Notes. Columns 3 and 5 are the seeing in *B* and *V* measured as the average FWHM of stars in *B*- and *V*-band final stacked images. The last column lists the reference astrometric catalogue.

3. Data reduction

Image reduction and calibration are mainly based on ESO-MVM reduction package (also known as ALAMBIC). This is a multi-instrument reduction tool originally developed for the ESO/EIS

survey (Mignano et al. 2007). It has also been extensively used in the production of ESO Advanced Data Products, see for instance the 30 Doradus/WFI Data Release[3] or the GOODS/ISAAC Final Data Release (Retzlaff et al. 2010). The detailed description of the package and the documentation of the algorithm structure implemented in ESO/MVM are given in Vandame (2004). This section presents a summary of the main reduction steps and our add-ons to the original pipeline. The latest version of the ALAMBIC code and user manual can be downloaded at the ESO webpage[4]. Here we used a modified version of the code (kindly provided by Bouy and Vandame, see Bouy et al. 2015) that has been partially rewritten to take advantage of the most recent hardware and recent Linux libraries. There are configuration files for many optical and near-infrared ESO instruments, but OmegaCAM is not officially supported so far. We therefore created a new configuration file for OmegaCAM, using the instrument description given in the VST user manual.

The following subsections describe the main reduction steps. The only steps for which we had to develop integrations to ALAMBIC are the cross-talk correction, the gain-harmonisation, and the control procedure to check the quality of CCD 82.

We call the complete set of data taken in each photometric band for a single pointing data block (DB). A DB consists of five science, five twilight flat-field, and ten bias frames. Each DB has been reduced independently. This may slightly increase the computational time, because some targets have been observed during the same night and therefore it would have been possible to compute the master bias and flat-field frames only once. However, we preferred to reduce each DB independently because in this way implementing the reduction pipeline is much easier and linear. The calibration stacking process is not very time consuming, therefore our choice has a negligible influence on the overall computational efficiency of the reduction process. A typical reduction run for a DB takes about 40 min on an Intel i7 3.4 GHz computer with 16 Gb of RAM.

3.1. Data organisation

First of all, the multi-extension raw image files are split, resulting in 32 single-extension files, corresponding to the 32 OmegaCAM detectors. Images are then classified and grouped together using the information stored in the file headers. ALAMBIC creates lists of images corresponding to consecutive observations of the same field taken with the same filter, called *observation blocks*. These are used to produce the *calibration blocks*, i.e. lists used to create the calibration images – bias, flats, illumination maps – and the *reduction blocks*, i.e. lists of science observations of each scientific target with the same filter.

3.2. Cross-talk

According to the OmegaCAM user manual, four detectors (CCDs 93-96, see Fig. 1) suffer electronic cross-talk. The strongest effect, of the order of a few percent, is between CCDs 95 and 96, while it is much lower for all the other CCDs. After a few tests we confirmed the cross-talk for CCDs 95 and 96 and we found that it is negligible in all other cases. The cross-talk was estimated by cross-correlating the signal registered on the same pixel in each pair of CCDs. As an example, Fig. 4

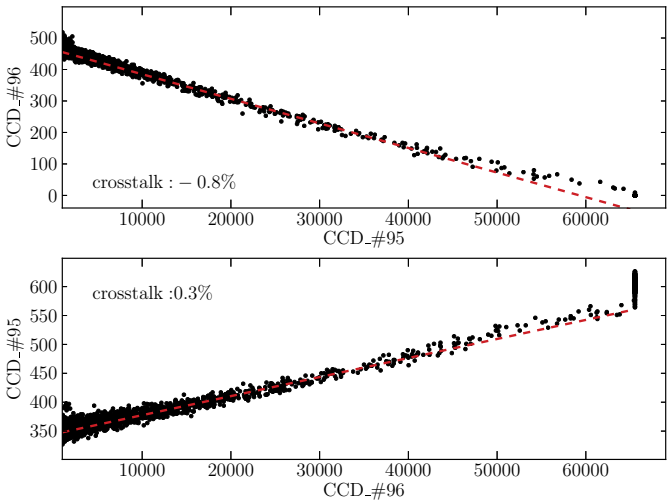

Fig. 4. Cross-talk effect between CCDs 95 and 96. Each point is the count in one pixel in the raw frame of the receiver CDD as a function of the count in the same pixel in the emitter. There is positive cross-talk from 96 to 95 (∼0.3%) and negative cross-talk from 95 to 96 (∼−0.8%). Only data-points corresponding to more than 2500 ADUs in the emitter are plotted.

shows the effect in a raw image of one of our science frames. The mean background level for this image is ∼480 ADUs in CCD 96 and ∼350 ADUs in CCD 95. When a bright source increases the signal in CCD 96, a signal above the background is registered in CCD 95 (see lowest panel in Fig. 4); the difference between the registered signal and the average background in one detector is proportional to the signal in the other one. Figure 4 shows deviations from the linear relation when the signal is above ∼50 000 ADUs. This is mainly due to the non-linearity of the detectors. This non-linearity can be safely ignored, since it only affects a few pixels in each image. We also note that the cross-talk effect of saturated stars in CCD 95 inversely saturates CCD 96 at 0 ADU. To avoid this problem, on September 12, 2012 the bias level of CCD 96 was increased to 650 ADU.

Since ALAMBIC does not include any cross-talk analysis, we developed a fast and easy procedure to calculate and correct for cross-talk. We assumed that the *observed* image is equal to

$$S_r = I_r + \alpha_r^e \cdot S^e, \quad (1)$$

where S_r and I_r are the observed and the *real* –that is, if no cross-talk were present– signal in the receiver, and S^e is the observed image in the emitter detector. α_r^e is the cross-talk coefficient between the receiver and the emitter CCDs. The coefficient was obtained by fitting a linear relations to the data points in Fig. 4. In all our images the coefficients for CCDs 95 and 96 are very similar, $\alpha_{96}^{95} \simeq -0.8\%$ and $\alpha_{95}^{96} \simeq 0.3\%$. These values were then used to correct the images, inverting Eq. (1). Figure 5 shows the very good results obtained with our procedure.

3.3. Stacking of calibration frames

During this phase of the reduction process, all calibration images of a given science reduction block are stacked together and the corresponding master bias and twilight flat images are produced. During this step, a bad-pixel detection procedure is applied and weight maps for flat-field images are computed. Details about the algorithm are given in the ALAMBIC user manual.

[3] http://archive.eso.org/archive/adp/ADP/30_Doradus/
[4] http://archive.eso.org/cms/eso-data/data-packages/eso-mvm-software-package.html

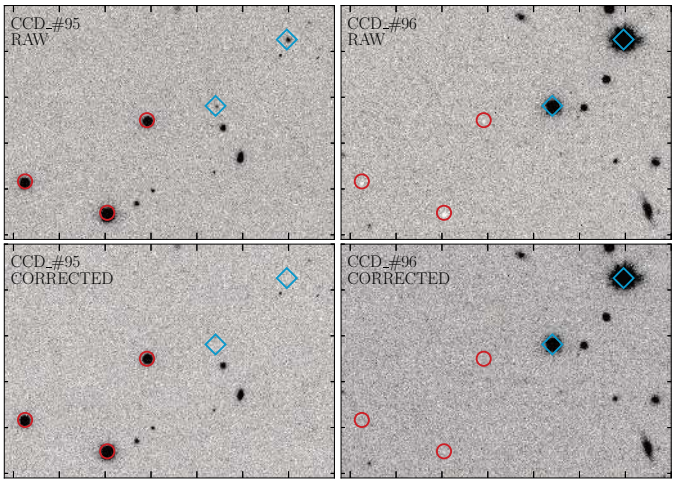

Fig. 5. Cross-talk effect between CCDs 95 and 96. The *top panels* show how bright sources in CCD 96 produce a positive signal in CCD 95, while bright sources in CCD 95 generate "holes" in CCD 96. The corrected images are shown in the *bottom panels*. Circles and diamonds mark the position of bright sources in CCDs 95 and 96, respectively. Fake sources are removed from the image in the *lower-left panel*, holes are removed from the image in the *lower-right panel*.

3.4. Gain harmonisation

The electronic converters of each detector are different, and each CCD may have a different efficiency. Therefore, each detector has its own effective gain and, as a consequence, its own photometric zero-point. The chip-to-chip gain variation quoted in the OmegaCAM user manual is of the order of 10%, resulting in a chip-to-chip zero-point scatter of ~0.1 mag. The procedure adopted by ALAMBIC to correct for this is to apply a multiplicative calibration constant to the master flats. The calibration is based on the analysis of a scientific image. The chip background is computed for each of the four borders of each chip in a narrow stripe. Then the chip-to-chip gain variations are calculated by comparing the values of each pair of adjacent stripes on different chips. As an example, in the case of a camera with 4×2 CCDs such as the WFI camera at the MPG/ESO 2.2 m telescope, the total number of equations, one for each pair of stripes, is ten, and the unknown parameters are the seven unknown flux-scales (this is a relative calibration). In this way, it is possible to obtain a robust calibration even if the sky background is not constant and presents some gradients for example.

The central vignetting cross does not allow using the standard ALAMBIC procedure for gain harmonisation. Given the high flux loss in a wide cross-shaped region at the centre of the FOV of the camera, it is not possible to easily connect the background values of adjacent regions of different CCDs affected by the central vignetting. We therefore developed a variation of the original ALAMBIC procedure optimised for our specific OmegaCAM observations. First of all, we note that the background level in our pre-reduced images (i.e. corrected for bias and flat field) does not show any significant gradient within each single detector. We can therefore assume a constant sky background across the whole FoV. We took one of the detectors as a reference and scaled the master flat-field image of the other 31 according to the ratio of the mean background values for each CCD on a science image. We recall that the reduction process is done independently for each DB, and hence this process was also repeated for each OmegaWINGS field in each filter. This procedure can be used since none of our science images are extremely crowded. The background estimation, and consequently the gain-harmonisation, would not have been possible otherwise, as in the case of observations of giant nearby galaxies with sizes of the order of one OmegaCAM CCD, for instance, or observations of the central regions of galactic globular clusters, nearby resolved galaxies, or other crowded stellar fields. In these cases it would be difficult – if not impossible – to estimate the sky background in each detector.

When the re-scaled master flat-field images are used to calibrate scientific images, the chip-to-chip gain variation is corrected and the resulting calibrated images therefore have a uniform background value. The quality of this procedure is be discussed in the following sections, in the context of the discussion of the overall photometric performances of our reduction pipeline.

To conclude this section, we add an important note about CCD 82 (its location in the OmegaCAM mosaic is shown in Fig. 1). The OmegaCAM user manual reports day-to-day gain variations of a few percent since the start of the OmegaCAM operations. We note that there are serious problems on CCD 82 for many observations. The background value is not constant, showing strong discontinuities in the form of horizontal stripes with different background values. The position and extension of these stripes are in general different from one image to the other, even for consecutive observations within the same DB. For this reason, we decided to discard all CCD 82 data when one scientific image in the DB was affected by this problem. We implemented in the pipeline a simple script to test whether the CCD 82 background is stable. If this is not the case, all CCD pixels are assigned a null weight. On June 2, 2012 ESO changed the video board connected to CCD 82 to fix this problem.

3.5. Illumination correction

A well-known problem that in particular affects wide-field cameras is the sky-concentration, a stray-light component which is centrally concentrated. This mostly affects observations with extremely bright background. In particular, flat-field frames are the most exposed to this effect. The net result, when flat-field exposures are applied without any correction, is an erroneous apparent trend of photometric zero point with distance from the centre of the camera FOV.

A common technique used to correct for this effect is to compute an illumination map to be applied to the flat-field frames to obtain *photometrically flat* reduced science frames. ALAMBIC implements an algorithm for computing and applying the illumination map, which is based on a sequence of dithered observations of the same stellar field. Basically, these images are reduced using the *normal* flat field, and photometric catalogues are extracted for each image. Since each star will be placed at a different position in each image, it is possible to map the zero-point variations as a function of the position on the focal plane. This is done using a least-squares estimator with rejection approximating the illumination map with a 2D polynomial function. This map is finally multiplied by the flat-field frame. A detailed description of the algorithms is given in Vandame (2002).

To compute the illumination map, we observed a well-populated stellar field, namely the Landolt SA107. We obtained five images in both the *B* and *V* band, using a dithering path wide enough to obtain observations of the same stars in different positions in the OmegaCAM focal plane. An outline of the dithering pattern is shown in Fig. 6. These observations were used to compute the illumination map, using a fourth-order polynomial

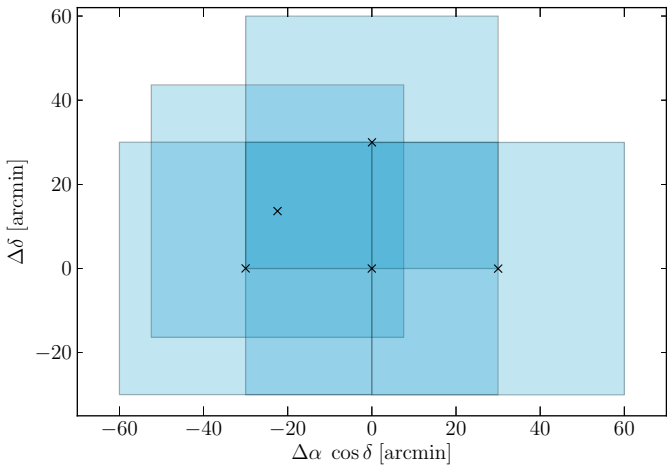

Fig. 6. Dithering pattern used for the observation of the SA107, which has been used to compute the illumination map. Crosses mark the five centres of the pointings, while the rectangles represent the OmegaCAM FoV.

function. This illumination-correction map was then applied to the flat-field frames used to calibrate all science frames.

In wide-field instruments, the illumination variation pattern across the large detector block can vary with time, telescope position, etc. The OmegaCAM consortium reported a dependence of the OmegaCAM illumination map on the telescope rotator angle[5]. It has been pointed out, however, out that to achieve a photometric accuracy at the 1% level, the illumination map can be considered "*stable on a timescale of at least 7 months*". Our illumination map was computed from observations taken in July 2012, one year after the first OmegaWINGS observation and one year before the last one. To check the stability of our illumination correction, we compared OmegaWINGS photometry with that of WINGS and SDSS and found no relevant variation of the photometric zero point across our images (see Sect. 5).

3.6. Stacking of science frames

During this stage, the pipeline finally operates on the science frames, using the calibration frames obtained from the previous steps. As part of this reduction stage, our pipeline computes and subtracts the additive sky background contribution from the images. This must be done since there are stray-light components mainly due to reflections that are caused by the segmented filters. This effect can be seen in the left panel of Fig. 7, where a *V*-band image obtained by stacking all observations of A2415 is shown. Only bias-subtraction and flat-field correction was been applied to these images, which were then stacked together without any further processing. For the sake of clarity, only a 5000 × 3500 pixel region is displayed. It nearly corresponds to the upper-left quadrant of the mosaic (CCDs 82, 83, 84, 90, 91, 92, see Fig. 1). An excess of light due to light scattered by the filter support is clearly visible on the right side of the image on the left panel. In addition, there are small discontinuities in the lower half of the images. These are the footprints of the borders of individual detectors on the five stacked images. These discontinuities are likely due to an imperfect flat-field correction. It is worth noting, however, that the image in Fig. 7 is displayed using a power-law gamma correction that strongly enhances the low-brightness details. These discontinuities are of the order of the standard deviation of the background signal. If these discontinuities were due to small uncertainties in the flat fielding, they should have been corrected as a multiplicative component. This is not the case; in fact, our sky-subtraction procedure eliminates them from the final stacks (as can be seen in the right panel of Fig. 7). This means that they are considered as additive contribution. This possible mis-interpretation would introduce a minor bias in the photometric zero-point in the regions of the mosaic corresponding to the CCDs borders. Considering their limited extension, and the fact that they are only present in a few images, the reason for which is not completely clear, they can be ignored because they will not affect the quality of the photometric calibration at levels higher than a few percent, which is the requirement for our scientific programme.

The additive stray-light component would not be a problem for stellar photometry, but we must correct for it since we are interested in surface photometry of extended sources. First of all, a standard calibration of the science frames is performed. Over- and pre-scan regions are trimmed from raw images, these are then bias-subtracted and flat-field corrected.

Then, the sky background is computed assuming that it is constant for the five consecutive images belonging to the same DB. Under this assumption, it can be computed with an algorithm similar to the one commonly used to remove the background from infrared observations or to correct for fringing patterns; we used the ALAMBIC fringing map estimator, fully described in the ALAMBIC user manual. Further details of the algorithms are also given by Vandame (2004).

The astrometric calibration is performed for all frames using as reference the 2MASS catalogue (Skrutskie et al. 2006) or the SDSS DR8 (Aihara et al. 2011), when available. Astrometric distortions are mapped using a polynomial function of order four. The absolute accuracy measured on the final stacked mosaic is of the order of 0.″2 and 0.″07 when the calibration is based on 2MASS and SDSS, respectively.

Satellite tracks are detected using a Hough-transform algorithm to search for straight lines in raw images. These are masked and flagged as bad pixels.

All images are then warped using the astrometric solution and projected in a user-defined common grid. We defined a distortion-free grid with a constant pixel scale equal to the average OmegaCAM pixels scale, that is 0.″213. The grid is centred at the target cluster centre. All warped images are finally stacked together using the weight maps. The output is the final stacked mosaic and the corresponding weight map. We note that since we used the same reference grid for *B*- and *V*-band images, the two output mosaics for each cluster are already aligned.

4. Photometric catalogues

4.1. Source extraction

The source extraction and measure of photometric and structural parameters was performed using SEXTRACTOR (Bertin & Arnouts 1996). *B*-band photometry was carried out with Sextractor *dual-mode*, using *V*-band image as reference. The catalogues extracted from *B*- and *V*-band images were then matched using a searching radius of 2″. We used a local background estimate with a size of 64 pixels and a detection threshold of 1.5σ above the background. In the following we list the parameters we measured. For a detailed description of the

[5] http://www.eso.org/sci/facilities/paranal/instruments/omegacam/doc/OCAM_illum.pdf

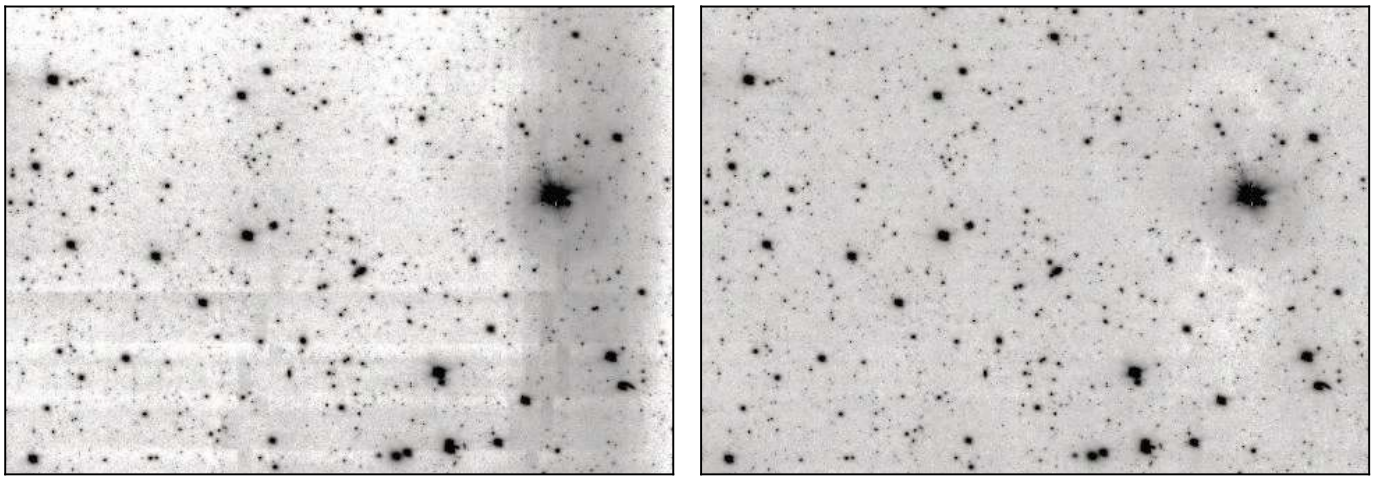

Fig. 7. Zoom of a 5000×3500 pixel region of two V-band stacked images of A2415 obtained using different procedures. The sky background has not been subtracted in the image in the *left panel*. The final product of our pipeline is shown in the *right panel*.

algorithm used to derive them we refer to the Sextractor user manual[6].

`RA`, `DEC`: equatorial coordinates of the barycentre of the source emission profile;
`RA_PEAK`, `DEC_PEAK`: equatorial coordinates of the source emission peak;
`X`, `Y`,`X_PEAK`, `Y_PEAK`: coordinates on the image, in pixels, of source barycentre and emission peak;
`ISOAREA_IMAGE`: isophotal area;
`KRON_RADIUS`: Kron radius;
`FWHM_IMAGE`: full width at half maximum;
`A_IMAGE`, `B_IMAGE`: semi-major and semi-minor axes. This was used to compute the axial ratio b/a;
`THETA_IMAGE`: position angle with respect to the north and measured counter-clockwise;
`CLASS_STAR`: stellarity index;
`MU_MAX`: surface brightness of the brightest pixel;
`MAG_ISO`: isophotal magnitude, defined using the detection threshold as the lowest isophote;
`MAG_ISOCOR`: Isophotal magnitude corrected to retrieve the fraction of flux lost by isophotal magnitudes by assuming Gaussian intensity profiles. As reported in the Sextractor user manual, *"this correction works best with stars; and although it is shown to give tolerably accurate results with most disk galaxies, it fails with ellipticals because of the broader wings of their profiles"*;
`MAG_AUTO`: Kron-like aperture magnitude. This is the most precise estimate of total magnitudes for galaxies;
`MAG_APER`: aperture magnitude. We used apertures with diameter 5, 10, 15, and 20 pixels; 1.″60, 2.″00, and 2.″16; 4, 10 and 20 kpc. To calculate the last three apertures we used the cluster distance listed in the WINGS database (Moretti et al. 2014).

4.2. Photometric calibration

Photometric calibration was made using WINGS stars as local standards. We fitted the equations

$$B_{\rm STD} - b = a_B\,(B-V)_{\rm STD} + b_B \quad (2)$$

$$V_{\rm STD} - v = a_V\,(B-V)_{\rm STD} + b_V. \quad (3)$$

[6] http://www.astromatic.net/software/sextractor

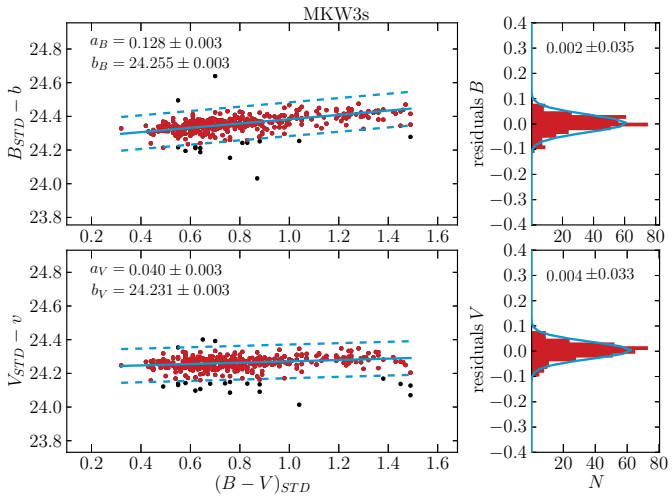

Fig. 8. Example of the photometric calibration fit obtained for all stars in common with previous WINGS photometry. In this example we used data from MKW3s observations. The *left panels* show the difference between calibrated WINGS INT photometry and instrumental OmegaCAM magnitudes as a function of the $B-V$ colour. The *upper and lower panels* show the results for B- and V-band photometry, respectively. The linear fit shown as a blue line was obtained by clipping out outliers (black dots). The distribution of the residuals is well described by a Gaussian function, shown in the *right panels*.

The data were fitted by imposing the condition that the colour-term (a_B and a_V) is constant within each ESO observing semester. As an example, Fig. 8 shows the calibration relation fitted to MKW3s data. The results for all OmegaWINGS clusters are listed in Table A.1. Colour term variations are within 0.015 mags.

4.3. Star-galaxy classification

The classification of OmegaWINGS sources was made following the method and criteria used for the original WINGS survey, as described in Varela et al. (2009). As a starting point, we classified objects on the basis of the Sextractor `CLASS_STAR` parameter:

stars : `CLASS_STAR`≥ 0.8

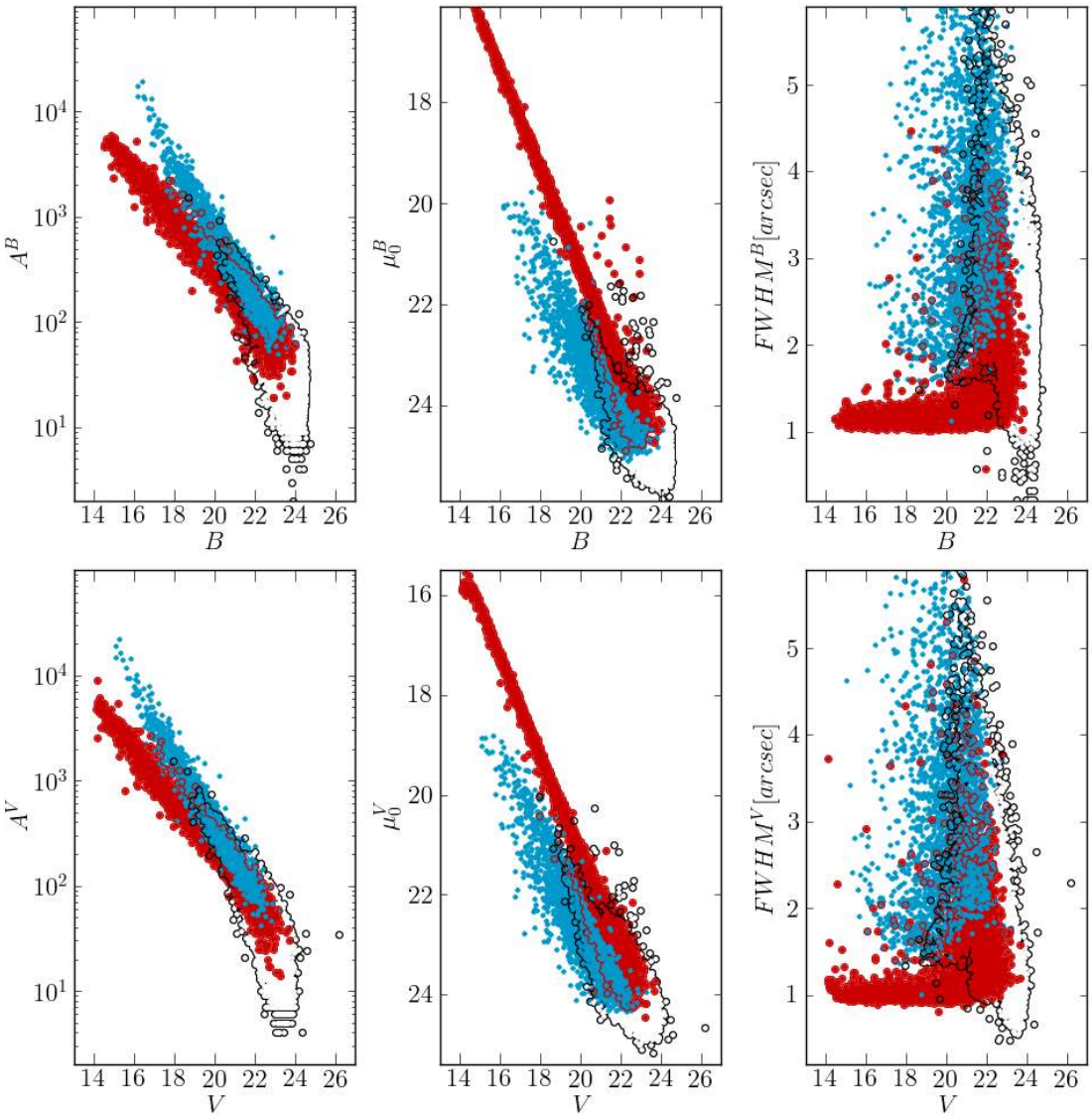

Fig. 9. Some of the plots used to classify sources in A3809, see text for details. Since blue dots (galaxies) are plotted on top of red ones (stars), we use red contours to mark (and delimit) the hidden regions occupied by stars. Similarly, black contours define the region where unclassified sources (not individually plotted) are located.

galaxies : CLASS_STAR$\leq$ 0.2
unknown : 0.8 <CLASS_STAR< 0.2

We then used a set of diagnostic plots, using different combinations of Sextractor parameters to check the result and correct any misclassification, if necessary. As an example, in Fig. 9 the isophotal area (A^B, A^V), the central surface brightness (μ_0^B, μ_0^V), and the FWHM of sources in the A3809 field are plotted as a function of the total magnitude in both the B- and V-bands. Other parameters used for the diagnostic plots include the ellipticity and the difference between aperture photometry at 5 and 15 pixels. We visually checked all clusters for outliers in the diagnostic plots, i.e. sources mis-classified on the basis of the automatic classification based on CLASS_STAR. For some of them we could safely redefine the star-galaxy classification after a careful visual inspection of their B- and V-band images. In some cases of faint and/or compact sources, B- and V-band photometry provided a different classification; in these cases we based our classification on the results provided in the band observed under the best seeing conditions. For some of the faintest objects, with properties between those of stars and galaxies, the classification remains *unknown*. The reliability of our classification is be analysed in Sect. 5. During the visual inspection of the diagnostic plots, we removed saturated stars from our catalogues.

4.4. Data retrieval

All SEXTRACTOR measurements for all galaxies are publicly available at CDS as a single table; a unique ID is assigned to each galaxy. To this end, we cross-matched the OmegaWINGS catalogue with the WINGS database (Moretti et al. 2014). For galaxies already in the WINGS database we took the WINGS-ID, while we defined a new ID for all other galaxies. A list of the columns of the catalogue is given in Table A.2. The full OmegaWINGS catalogue will be included in the next release of the WINGS database. This is planned at the end of our AAOmega spectroscopic survey. We note, however, that the OmegaWINGS catalogue at CDS, as any other CDS table, is already part of the VO and can therefore be easily cross-matched with the WINGS database using any VO tool, for example STILTS.

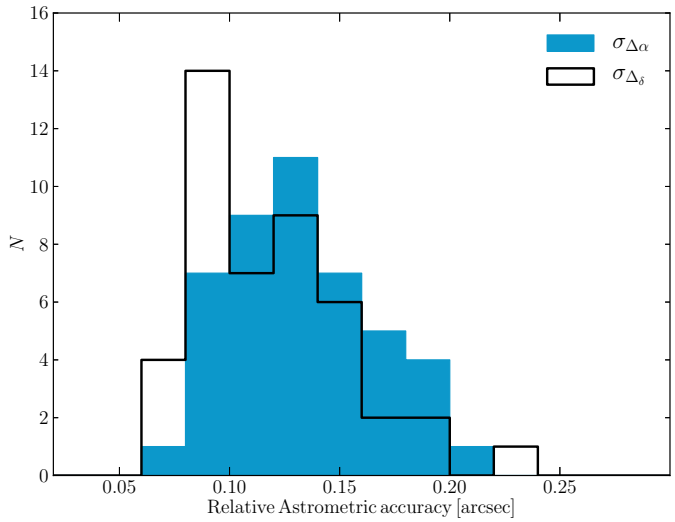

Fig. 10. Dispersion of the distributions of sky-coordinate differences between OmegaWINGS and WINGS positions of all stars in each 46 OmegaWINGS fields. Only stars brighter than $V = 20$ were used.

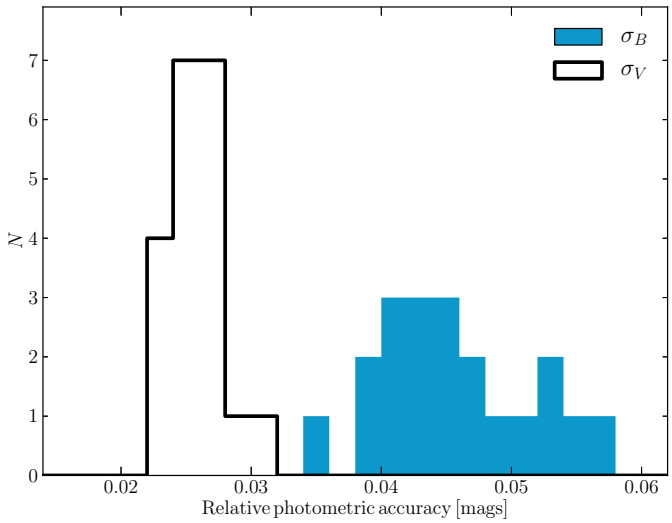

Fig. 11. Relative photometric accuracy based on a comparison with SDSS DR9. The histograms shows the dispersion of the distributions of differences between OmegaWINGS and SDSS photometry.

5. Data reduction quality checks

5.1. Astrometry

The astrometric accuracy of our catalogues was tested against the 2MASS and SDSS DR8 (when available) stellar catalogues. By comparing the difference in the source positions, we verified that no residual distortions are present in the final mosaics. The absolute astrometric accuracy is well within the precision required for the purposes of our scientific project. For each cluster in our sample, we compared OmegaWINGS sky coordinates of all stars in the FOV with those of 2MASS or SDSS (depending on the catalogue used as the astrometric reference). The distributions of the differences in α and δ coordinates have always negligible mean values and typical dispersions of $0\farcs2$ (2MASS) and $0\farcs07$ (SDSS). As an additional test of the astrometric calibration accuracy, we compared the sky-coordinates of all stars in OmegaWINGS and WINGS catalogues. The dispersion of the $\Delta\alpha$ and $\Delta\delta$ distributions is a robust indicator of the accuracy of our astrometric calibration, as WINGS was calibrated independently. Results are shown in Fig. 10 and confirm that the internal astrometry calibration is accurate at a level always better than $0\farcs2$[7]. The mean values of the distributions are $\simeq 0\farcs1$ for both right ascension and declination.

We finally note that the internal accuracy of the catalogues used as reference in this section are very close to the measured dispersions, that is $\sim 0\farcs2$, $\sim 0\farcs1$, and $\sim 0\farcs07$, when comparing OmegaWINGS astrometry with 2MASS, WINGS, and SDSS, respectively. We can therefore conclude that our astrometric calibration has an internal accuracy at the level of at least $0\farcs1$.

5.2. Photometry

The relative accuracy of OmegaWINGS photometry across the OmegaCAM FoV was tested by comparing OmegaWINGS photometry with that of SDSS. We adopted the linear colour equations proposed by Jordi et al. (2006) to transform SDSS *ugr* photometry into standard *BV* magnitudes. For each of the 20 OmegaWINGS fields observed by SDSS, we calculated the dispersion of the differences between OmegaWINGS and (transformed) SDSS magnitudes for all stars with $B < 20$ mag and $V < 19$ mag. Results are shown in Fig. 11. In the V band the relative photometric accuracy is $\lesssim 0.03$ mag for all clusters. The dispersions of ΔB are 0.04–0.06 mags. The systematically higher dispersion in the B band are due to non-linear colour terms in the transformations from SDSS *ugr* to *BV* photometric systems and/or a dependence of the transformations on stars metallicity or colour (Jordi et al. 2006). In Sect. 4.2 we found no high-order colour term in the comparison of OmegaWINGS photometry with that of WINGS. A detailed discussion of this problem is beyond the aim of this paper.

To check the spatial stability of OmegaWINGS calibration, we analysed the magnitude difference between OmegaWINGS and (transformed) SDSS photometry as a function of the position in the mosaic. As an example, the magnitude difference of all stars with $V < 19$ in Z8852 are shown in the right panel of Fig. 12. For comparison, the same comparison when no illumination correction is applied (see Sect. 3) is shown in the left panel of Fig. 12. The strongest effect of the illumination correction, from the edge to the centre of the mosaic, is ~ 0.2 mag. We analysed the same maps as were shown in Fig. 12 for all 20 OmegaWINGS fields with available SDSS photometry in B and V band and conclude that the photometric zero-point in all calibrated catalogues is constant across the whole mosaic and that there are no residual systematic effects of the illumination correction or the gain harmonisation.

Finally, the sky-subtraction procedure was tested by performing a detailed analysis of the radial profiles of a few extended bright galaxies and comparing the results obtained from the final OmegaCAM stacked mosaics with data from the WINGS survey. As an example, in Fig. 13 the comparison of OmegaWINGS and WINGS images of a region populated by several galaxies shows that the structure of the galactic haloes is the same in the two images. This is a clear indication that the sky-subtraction procedure did remove all large-scale artefacts from the images (see Fig. 7), but it did not alter the galaxy profiles. A more quantitative analysis of this point can be derived

[7] The internal accuracy of WINGS astrometry is $\sim 0\farcs2$ (Fasano et al. 2006); values in Fig. 10 are therefore upper limits of the OmegaWINGS astrometric calibration uncertainties.

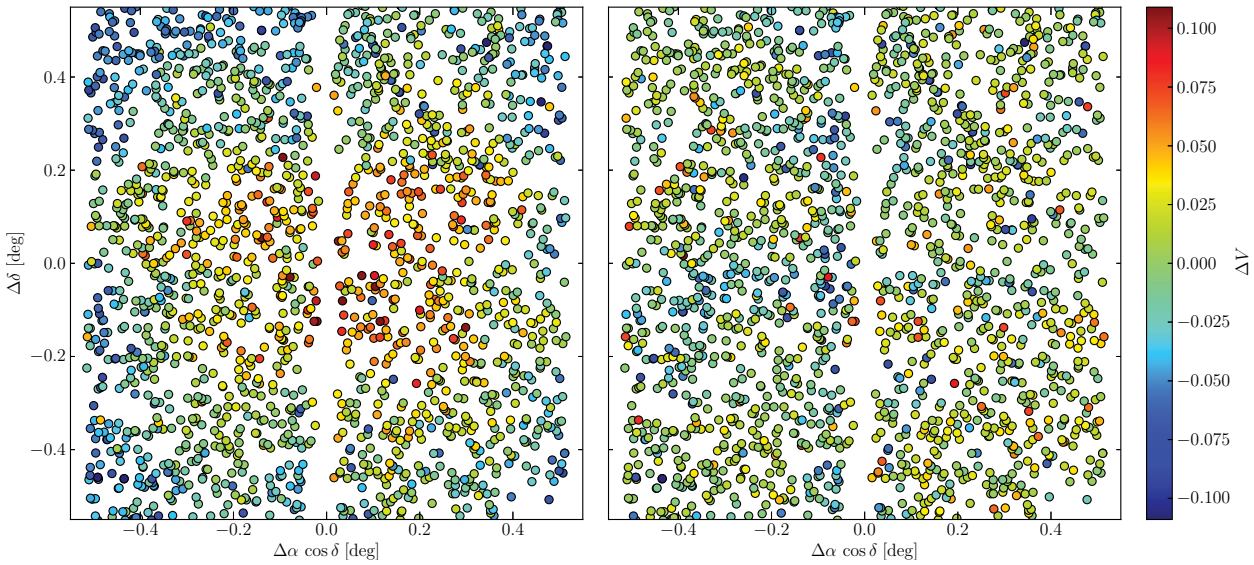

Fig. 12. Magnitude difference between OmegaWINGS and SDSS photometry transformed into the Johnson's system for stars brighter than $V = 20$ mag as a function of the position on the OmegaWINGS detector. In the *right panel* the result is obtained from the final OmegaWINGS calibrated catalogue, while the photometry in the *left panel* was obtained with no illumination correction.

from the direct comparison of radial profiles of the same galaxy obtained from OmegaWINGS and WINGS images, as the one presented in Fig. 14. The profile obtained from OmegaCAM image perfectly agrees with the one obtained at the INT telescope, out to the detection limit, corresponding to a radius of ∼16″, that is 75 pixels in OmegaCAM. The minor differences in the central regions are due to the fact that OmegaWINGS V-band observations of A2457 were carried out under better seeing conditions (1.″1) than those of WINGS (1.″4).

5.3. Photometric completeness

The overall OmegaWINGS photometric completeness factor was estimated by comparing the magnitude distributions (MD) of all sources in OmegaWINGS and WINGS catalogues. To perform the comparison, the WINGS distribution was renormalised to match the total number of OmegaWINGS sources with $16 < V < 21$ mag. The MDs obtained for all 45 OmegaWINGS fields are shown in Fig. A.1. The photometric depth depends on the seeing conditions during observations, but OmegaWINGS photometry is in general 0.5–1.0 mag shallower than that of WINGS. However, when OmegaWINGS observations were carried out with a seeing $\lesssim$1.″0, OmegaWINGS is as deep as (and in some cases deeper than) WINGS (see Fig. A.1). The overall photometric depth of OmegaWINGS was estimated by stacking together all 45 MDs. Figure 15 shows that OmegaWINGS MD peaks at $V \sim 22.5$ mag and that of WINGS at $V \sim 23.4$. The OmegaWINGS completeness can be estimated as the ratio of OmegaWINGS to WINGS MDs. The 50% completeness level is reached at $V = 23.1$ mag, the 80% level at $V = 22.4$ mag (see Fig. 15). This result is based on the assumption that WINGS photometry is complete at least up to $V \sim 23$ mag. We therefore performed an additional test by fitting an exponential relation to the bright tail of the histogram in Fig. 15. The completeness factor was obtained as the ratio of the observed MD to the best-fit exponential model. Following this approach, 50% and 80% completeness are found at $V = 23.3$ and 22.7 mag, respectively, confirming our previous results within reasonable uncertainties.

5.4. Star-galaxy classification

The quality of the OmegaWINGS source classification mostly depends on the seeing conditions during the B- and V-band observations. The fraction of objects that we were able to classify as galaxies or stars decreases at increasing magnitudes. We estimated the depth of our classification as the magnitude at which 50% of the sources in each cluster are classified. For most clusters we measured a magnitude $V \sim 22.0$ mag, or even fainter than this for clusters observed with good seeing. The worst cases are A970 and A2717, which were both observed with a seeing of 1.″6 and 1.″2 in B- and V-band, respectively. For these two clusters 50% of the detected sources are not classified at magnitudes fainter than $V \simeq 21.0$ mag. For clusters observed in both bands with 1″ seeing or better, the classification is reliable for 50% of the sources at $V \simeq 22.5$ mag. The results for all OmegaWINGS clusters are shown in Fig. A.2.

To check the reliability of OmegaWINGS source classification, we compared it with that of WINGS. For each cluster we divided the sources classified as galaxies in OmegaWINGS into three magnitude bins: $V < 20$ mag, $20 < V < 21$ mag, and $21 < V < 22$ mag. We then calculated how many OmegaWINGS galaxies were classified as galaxy, star, and unknown in WINGS. The histograms of these fractions are presented in Fig. 16. In all but two clusters, the fraction of bright ($V < 20$ mag) OmegaWINGS galaxies classified as galaxies in WINGS is >97.5%. In more than 50% of the clusters the number of faint OmegaWINGS galaxies with unknown classification in WINGS is negligible; in all other clusters, this fraction is still lower than 10% (see lower panel of Fig. 16). There are no OmegaWINGS galaxies with $V < 20$ mag classified as stars in WINGS in any cluster. The fraction of galaxies misclassified as stars in WINGS is also negligible (<5%) for fainter galaxies ($20 < V < 22$ mag). To summarise, we can conclude that the classification of galaxies in OmegaWINGS is highly reliable.

The other question we addressed with this analysis is the completeness of our classification, that is how many galaxies are missed by our classification? Clues on this question can be provided by studying OmegaWINGS classification of

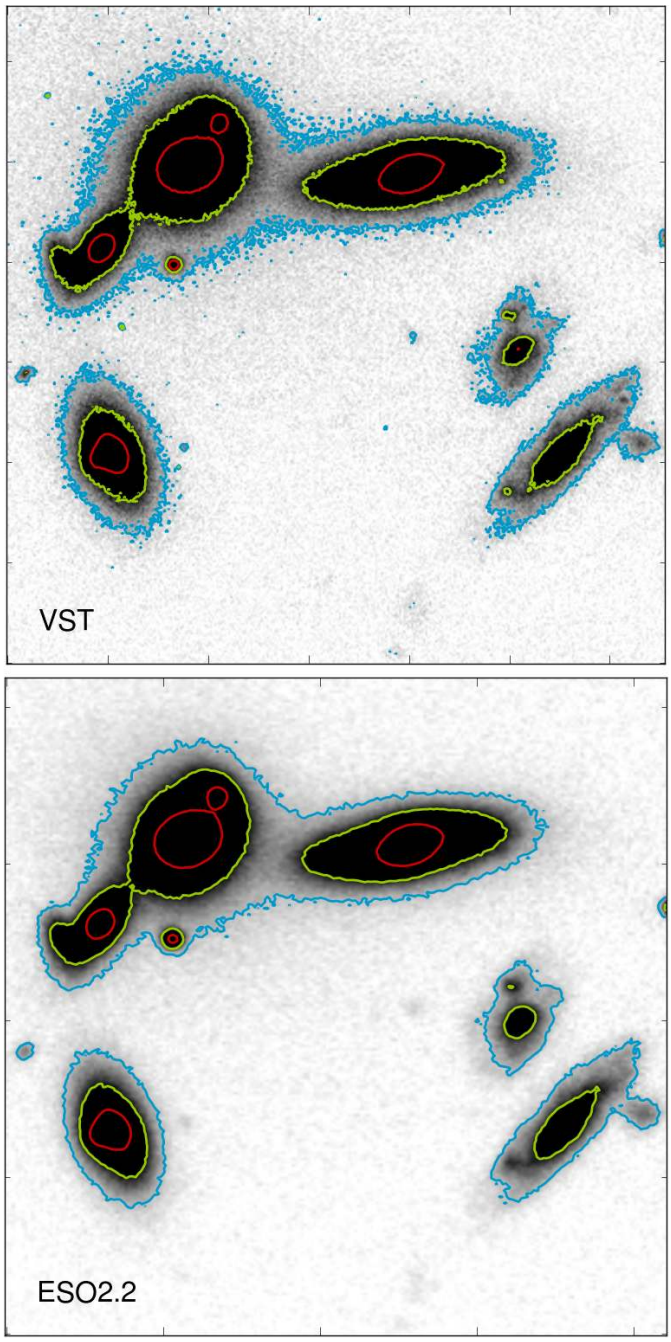

Fig. 13. Zoom on a 35″ × 35″ region in the *V*-band VST image of A151 and on the WINGS image, taken with the WFI camera at the MPG/ESO 2.2m telescope. The same contour levels are plotted in both images. Besides the slightly lower S/N of the VST image with respect to the MPG/ESO 2.2 m image, the shape and location of the contour is the same. This is an indication that the background subtraction did not alter the faintest structures in galaxy haloes.

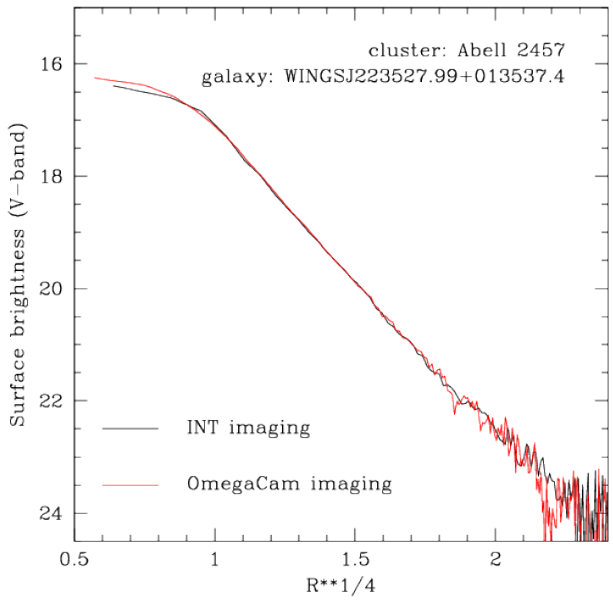

Fig. 14. Comparison of the major-axis surface brightness profile of a bright galaxy as obtained from the OmegaCAM and the WFC-INT images. The agreement of the two profiles demonstrates the reliability of our sky-subtraction procedure.

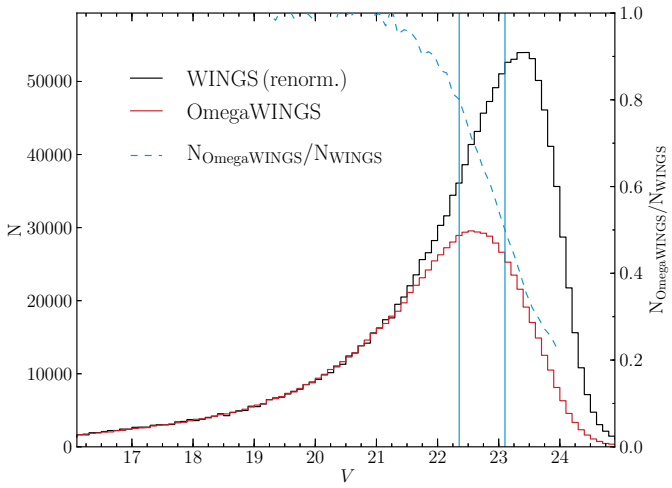

Fig. 15. *V*-band magnitude distribution of all objects in the OmegaWINGS and WINGS database. WINGS MD was re-normalised to match the total number of sources with 16 < *V* < 21 mag. The ratio of OmegaWINGS to WINGS MDs is shown as a dotted line; the corresponding scale is shown on the right-hand axis. The verticals are traced at the magnitude corresponding to a ratio of 0.5 and 0.8 (50% and 80% completeness level).

WINGS galaxies, shown in Fig. 17. In most clusters, all WINGS galaxies with $V < 20$ mag are also classified as galaxies in OmegaWINGS, there are bright WINGS galaxies that are otherwise classified in OmegaWINGS in just a few clusters; their fraction is always low (5%−10%), however. The number of WINGS galaxies with $21 < V < 22$ mag with unknown OmegaWINGS classification is not negligible in a significant number of clusters. Nonetheless, in ∼50% of the clusters the number of WINGS galaxies misclassified as stars in OmegaWINGS is 5−15%. The reliability of the source classification is strongly dependent on seeing conditions during the observations, and in fact, the clusters with the most relevant discrepancies between OmegaWINGS and WINGS classification are those with relevant seeing differences between the WINGS and OmegaWINGS observations.

To summarise, we conclude that the OmegaWINGS source classification is highly reliable for all objects with $V < 20$ mag. This is the magnitude range used to select the targets for our AAOmega spectroscopic follow-up survey. At faintest magnitudes, in clusters observed under poor seeing conditions, the OmegaWINGS galaxy selection is not complete, meaning that

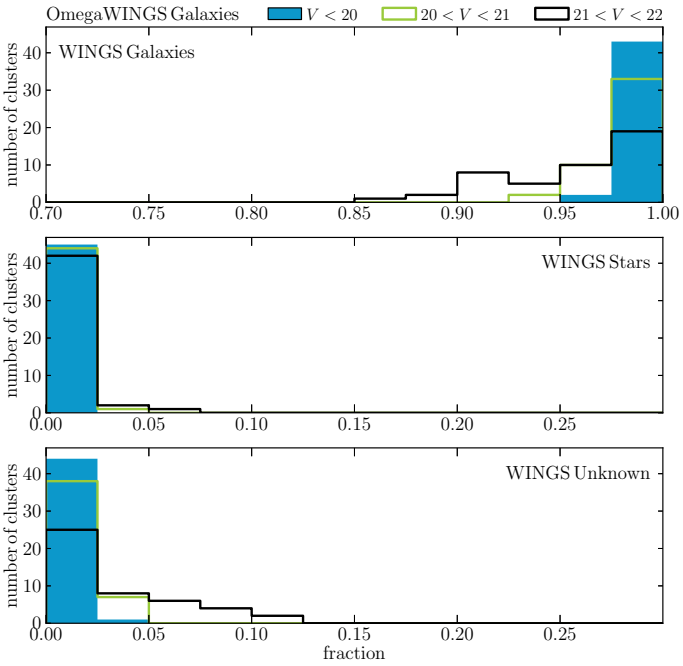

Fig. 16. Fraction of objects classified as galaxies in OmegaWINGS that have been classified as galaxies (*upper panel*), stars (*central panel*), or with unknown classification (*lower panel*) in WINGS. In each panel, the solid blue, green, and black histograms show objects in three different magnitude bins, as indicated in the legend.

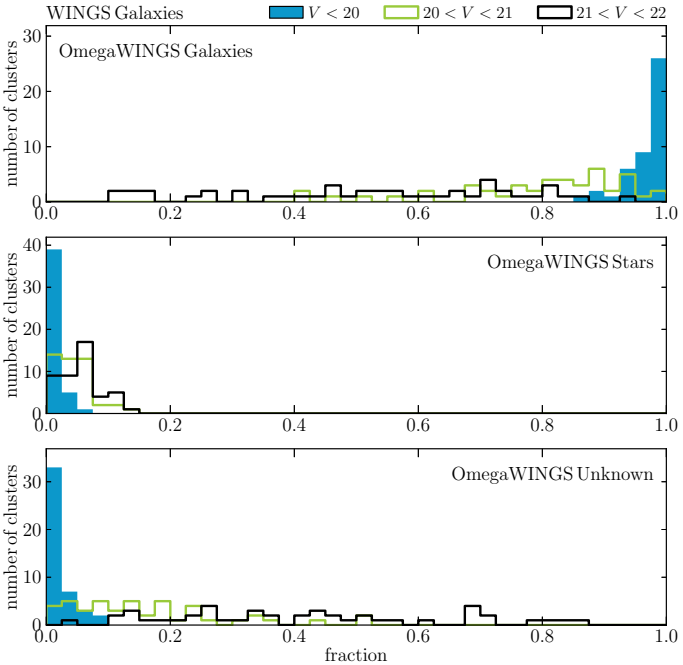

Fig. 17. Fraction of objects classified as galaxies in WINGS that have been classified as galaxies (*upper panel*), stars (*central panel*), or with unknown classification (*lower panel*) in OmegaWINGS. In each panel, the solid blue, green, and black histograms show objects in three different magnitude bins, as indicated in the legend.

a significant number of galaxies might be assigned an unknown classification. On the other hand, the classification of galaxies in OmegaWINGS is very robust and it is very unlikely that a OmegaWINGS galaxy is actually a star.

6. Summary

This paper is the first of a series presenting OmegaWINGS, the wider-field extension of the WINGS database for X-ray selected galaxy clusters at $z = 0.04$–0.07. The B- and V-band observations of the 46 WINGS clusters observed with OmegaCAM/VST are presented here, while the ongoing u-band OmegaCAM/VST and spectroscopic AAOmega/AAT follow-ups will be presented in subsequent papers.

All clusters were observed for 25 min in each band, with a median seeing of 1″ in B and V band, and <1.″3 and 1.″2 in 80% of the B- and V-band images, respectively. The data were reduced with a modified version of the ESO-MVM ALAMBIC reduction package, developing ad hoc cross-talk, gain harmonisation, and CCD control procedures. Special care was taken for illumination correction, using OmegaCAM observations of standard stellar fields.

Sextractor photometric catalogues were produced and are released with this paper at CDS. Catalogues and reduced images will also be part of the next release version of the WINGS database.

The quality of the astrometry, photometric accuracy, star-galaxy separation, and sky-subtraction were tested in various ways and show that results are generally of the same or even better quality than the previous WINGS results. The absolute astrometric accuracy is ∼0.″2 and 0.″07 when the calibration is based on 2MASS and SDSS, respectively. The photometric catalogues are 50% complete at $V = 23.1$ mag and 80% complete at $V = 22.4$ mag.

The B- and V-band OmegaCAM images have provided the AAOmega spectroscopic targets and were employed to identify jellyfish candidate galaxies that are subject to ram pressure stripping (Poggianti et al. 2015). The ongoing analysis of these images includes surface brightness analysis with GASPHOT (D'Onofrio et al. 2014) and a morphological classification with MORPHOT (Fasano et al. 2012). Taking advantage of the large clustercentric radii reachable for our clusters by the OmegaCAM imaging, we plan to use this dataset for studying the effects of the environment on galaxy properties out to large distances from the cluster centre, as well as for a number of studies on the dynamical status and light distribution of clusters.

Acknowledgements. We would like to warmly thank Hervé Bouy and Benoit Vandame for sharing their code and for the useful discussion. We acknowledge financial support from the PRIN-INAF 2010 and 2014. B.V. was supported by the World Premier International Research Center Initiative (WPI), MEXT, Japan and the Kakenhi Grant-in-Aid for Young Scientists (B)(26870140) from the Japan Society for the Promotion of Science (JSPS). This publication makes use of data products from the Two Micron All Sky Survey, which is a joint project of the University of Massachusetts and the Infrared Processing and Analysis Center/California Institute of Technology, funded by the National Aeronautics and Space Administration and the National Science Foundation. SDSS-III is managed by the Astrophysical Research Consortium for the Participating Institutions of the SDSS-III Collaboration including the University of Arizona, the Brazilian Participation Group, Brookhaven National Laboratory, Carnegie Mellon University, University of Florida, the French Participation Group, the German Participation Group, Harvard University, the Instituto de Astrofisica de Canarias, the Michigan State/Notre Dame/JINA Participation Group, Johns Hopkins University, Lawrence Berkeley National Laboratory, Max Planck Institute for Astrophysics, Max Planck Institute for Extraterrestrial Physics, New Mexico State University, New York University, Ohio State University, Pennsylvania State University, University of Portsmouth, Princeton University, the Spanish Participation Group, University of Tokyo, University of Utah, Vanderbilt University, University of Virginia, University of Washington, and Yale University.

Appendix A: Supplementary tables and figures

Table A.1. Photometric zero points and colour terms.

Cluster	a_B	b_B	a_V	b_V	P
A119	0.116 ± 0.004	24.291 ± 0.006	0.030 ± 0.004	24.291 ± 0.006	P88
A160	0.116 ± 0.004	24.405 ± 0.005	0.030 ± 0.004	24.295 ± 0.005	P88
A193	0.116 ± 0.004	24.367 ± 0.005	0.030 ± 0.004	24.313 ± 0.005	P88
A3128	0.116 ± 0.004	24.221 ± 0.004	0.030 ± 0.004	24.266 ± 0.004	P88
A3158	0.116 ± 0.004	24.312 ± 0.004	0.030 ± 0.004	24.213 ± 0.004	P88
A500	0.116 ± 0.004	24.145 ± 0.004	0.030 ± 0.004	24.226 ± 0.004	P88
A754	0.116 ± 0.004	24.320 ± 0.003	0.030 ± 0.004	24.340 ± 0.004	P88
A957x	0.116 ± 0.004	24.313 ± 0.005	0.030 ± 0.004	24.311 ± 0.005	P88
A970	0.116 ± 0.004	24.281 ± 0.004	0.030 ± 0.004	24.333 ± 0.004	P88
A1983	0.128 ± 0.003	24.297 ± 0.004	0.040 ± 0.003	24.250 ± 0.004	P89
A2382	0.128 ± 0.003	24.294 ± 0.003	0.040 ± 0.003	24.293 ± 0.004	P89
A2399	0.128 ± 0.003	24.357 ± 0.003	0.040 ± 0.003	24.267 ± 0.003	P89
A2415	0.128 ± 0.003	24.310 ± 0.003	0.040 ± 0.003	24.321 ± 0.004	P89
A2457	0.128 ± 0.003	24.316 ± 0.004	0.040 ± 0.003	24.287 ± 0.004	P89
A3556	0.128 ± 0.003	24.227 ± 0.003	0.040 ± 0.003	24.235 ± 0.003	P89
A3560	0.128 ± 0.003	24.299 ± 0.003	0.040 ± 0.003	24.217 ± 0.003	P89
A3809	0.128 ± 0.003	24.259 ± 0.003	0.040 ± 0.003	24.204 ± 0.003	P89
MKW3s	0.128 ± 0.003	24.255 ± 0.003	0.040 ± 0.003	24.231 ± 0.003	P89
A151	0.122 ± 0.003	24.316 ± 0.005	0.036 ± 0.004	24.229 ± 0.005	P90
A1631a	0.122 ± 0.003	24.377 ± 0.004	0.036 ± 0.004	24.285 ± 0.004	P90
A2593	0.122 ± 0.003	24.275 ± 0.004	0.036 ± 0.004	24.342 ± 0.004	P90
A3266	0.122 ± 0.003	24.259 ± 0.003	0.036 ± 0.004	24.249 ± 0.004	P90
A3395	0.122 ± 0.003	23.825 ± 0.003	0.036 ± 0.004	23.967 ± 0.003	P90
A3376	0.122 ± 0.003	24.233 ± 0.003	0.036 ± 0.004	24.164 ± 0.003	P90
Z8852	0.122 ± 0.003	24.310 ± 0.004	0.036 ± 0.004	24.261 ± 0.004	P90
A1069	0.133 ± 0.002	24.321 ± 0.003	0.044 ± 0.002	24.336 ± 0.003	P91
A147	0.133 ± 0.002	24.338 ± 0.004	0.044 ± 0.002	24.311 ± 0.004	P91
A168	0.133 ± 0.002	24.340 ± 0.005	0.044 ± 0.002	24.299 ± 0.005	P91
A1991	0.133 ± 0.002	24.304 ± 0.004	0.044 ± 0.002	24.283 ± 0.004	P91
A2107	0.133 ± 0.002	24.407 ± 0.003	0.044 ± 0.002	24.356 ± 0.003	P91
A2589	0.133 ± 0.002	24.326 ± 0.004	0.044 ± 0.002	24.324 ± 0.004	P91
A2657	0.133 ± 0.002	24.286 ± 0.004	0.044 ± 0.002	24.317 ± 0.004	P91
A2665	0.133 ± 0.002	24.333 ± 0.004	0.044 ± 0.002	24.295 ± 0.004	P91
A2717	0.133 ± 0.002	24.304 ± 0.005	0.044 ± 0.002	23.847 ± 0.005	P91
A2734	0.133 ± 0.002	24.343 ± 0.004	0.044 ± 0.002	24.296 ± 0.004	P91
A3528	0.133 ± 0.002	24.277 ± 0.002	0.044 ± 0.002	24.196 ± 0.002	P91
A3530	0.133 ± 0.002	24.298 ± 0.002	0.044 ± 0.002	24.231 ± 0.003	P91
A3532	0.133 ± 0.002	24.292 ± 0.002	0.044 ± 0.002	24.212 ± 0.003	P91
A3558	0.133 ± 0.002	24.253 ± 0.002	0.044 ± 0.002	24.223 ± 0.002	P91
A3667	0.133 ± 0.002	24.247 ± 0.002	0.044 ± 0.002	24.257 ± 0.002	P91
A3716	0.133 ± 0.002	24.311 ± 0.002	0.044 ± 0.002	24.265 ± 0.003	P91
A3880	0.133 ± 0.002	23.841 ± 0.004	0.044 ± 0.002	24.289 ± 0.004	P91
A4059	0.133 ± 0.002	24.286 ± 0.004	0.044 ± 0.002	24.250 ± 0.004	P91
A85	0.133 ± 0.002	24.372 ± 0.004	0.044 ± 0.002	24.315 ± 0.004	P91
IIZW108	0.133 ± 0.002	24.325 ± 0.002	0.044 ± 0.002	24.278 ± 0.002	P91

Table A.2. Description of the table available at CDS.

Column	Units	Description
WINGSID		Unique identificator
Cluster name		Name of host cluster
RA(J2000)	deg	Right Ascension of emission peak
Dec(J2000)	deg	Declination of emission peak
Area	arcsec^2	Isophotal area
KronRad	pix	Kron radius
FWHM	pix	Full width at half maximum along major axis
b/a		axial ratio
PA	deg	[–90/90] Position angle (North=0, Eastwards)
μ_B^0	mag arcsec^{-2}	B-band surface brightness of the emission peak
μ_V^0	mag arcsec^{-2}	V-band surface brightness of the emission peak
$B_{\rm ISO}$	mag	B-band SExtractor MAG_ISO
$V_{\rm ISO}$	mag	V-band SExtractor MAG_ISO
$B_{\rm ISOC}$	mag	B-band SExtractor MAG_ISOC
$V_{\rm ISOC}$	mag	V-band SExtractor MAG_ISOC
$B_{\rm AUTO}$	mag	B-band SExtractor MAG_AUTO
$V_{\rm AUTO}$	mag	V-band SExtractor MAG_AUTO
$B_{\rm 5pix}$	mag	B-band magnitude in aperture of 5 pixels
$V_{\rm 5pix}$	mag	V-band magnitude in aperture of 5 pixels
$B_{\rm 10pix}$	mag	B-band magnitude in aperture of 10 pixels
$V_{\rm 10pix}$	mag	V-band magnitude in aperture of 10 pixels
$B_{\rm 15pix}$	mag	B-band magnitude in aperture of 15 pixels
$V_{\rm 15pix}$	mag	V-band magnitude in aperture of 15 pixels
$B_{\rm 20pix}$	mag	B-band magnitude in aperture of 20 pixels
$V_{\rm 20pix}$	mag	V-band magnitude in aperture of 20 pixels
$B_{\rm fib1}$	mag	B-band magnitude in aperture of 1.″60
$V_{\rm fib1}$	mag	V-band magnitude in aperture of 1.″60
$B_{\rm fib2}$	mag	B-band magnitude in aperture of 2.″00
$V_{\rm fib2}$	mag	V-band magnitude in aperture of 2.″00
$B_{\rm fib3}$	mag	B-band magnitude in aperture of 2.″16
$V_{\rm fib3}$	mag	V-band magnitude in aperture of 2.″16
$B_{\rm 4kpc}$	mag	B-band magnitude in aperture of 4 kpc
$V_{\rm 4kpc}$	mag	V-band magnitude in aperture of 4 kpc
$B_{\rm 10kpc}$	mag	B-band magnitude in aperture of 10 kpc
$V_{\rm 10kpc}$	mag	V-band magnitude in aperture of 10 kpc
$B_{\rm 20kpc}$	mag	B-band magnitude in aperture of 20 kpc
$V_{\rm 20kpc}$	mag	V-band magnitude in aperture of 20 kpc
cl		source classification. 1:star; 2:galaxy; 3:unknown

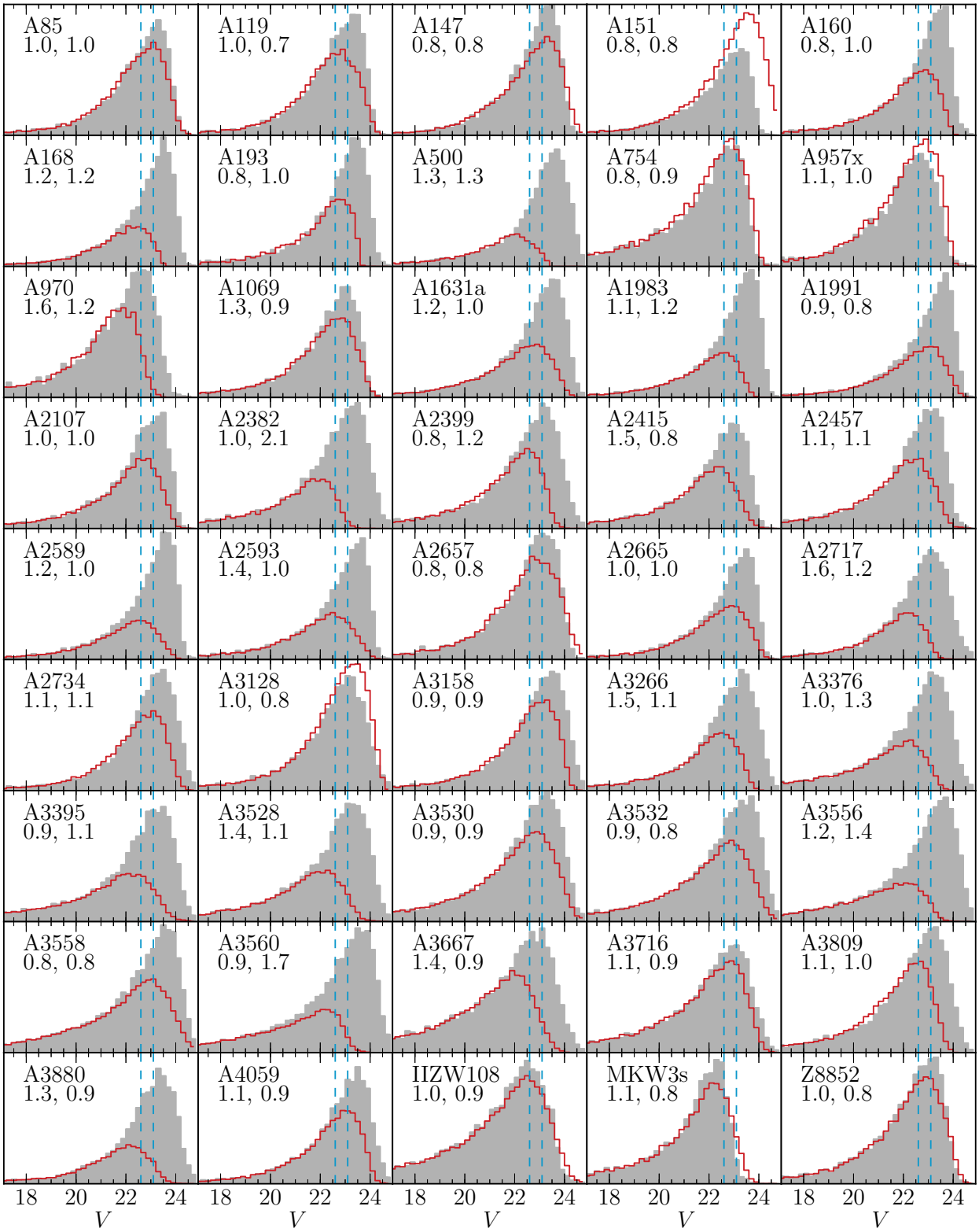

Fig. A.1. Magnitude distributions of all sources in OmegaWINGS (red histograms) and WINGS (shaded grey histograms) for all 45 OmegaWINGS fields. WINGS MDs are renormalised to match the number of bright ($16 < V < 21$ mag) objects in OmegaWINGS LFs. The vertical lines show the overall OmegaWINGS 50% and 80% completeness level (see Sect. 5.3). The label in each panel indicates the seeing in *B*- and *V*-band images, in arcseconds.

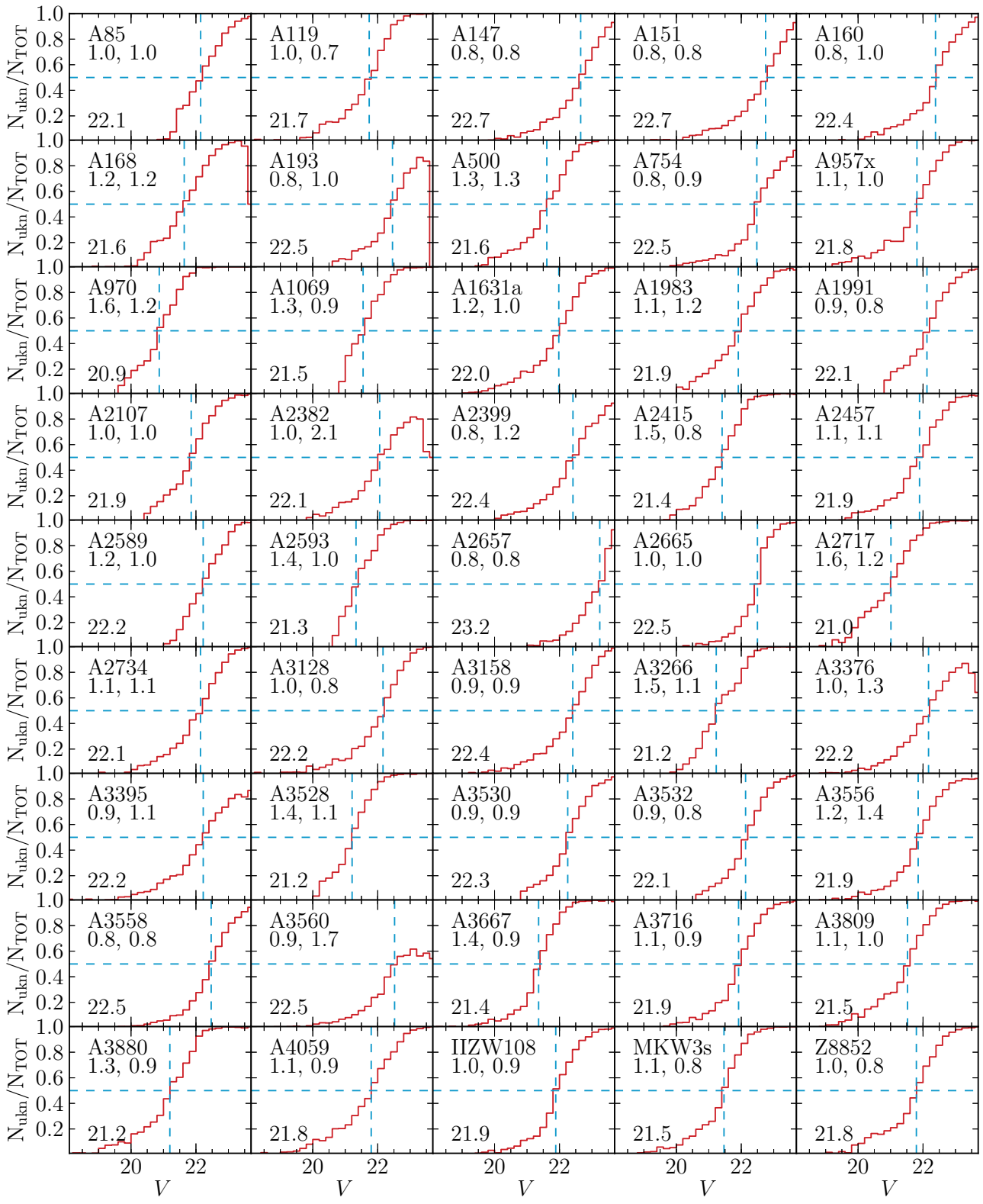

Fig. A.2. Fraction of sources with unknown classification in all OmegaWINGS clusters as a function of *V*-band magnitude. The magnitude at which 50% of sources are un-classified is shown by the dashed lines and is indicated in the lower left corner of each sub-panel. The label in the upper left corner of each panel indicates the seeing in *B*- and *V*-band images, in arcseconds.

References

Aihara, H., Allende Prieto, C., An, D., et al. 2011, ApJS, 193, 29
Bahé, Y. M., McCarthy, I. G., Balogh, M. L., & Font, A. S. 2013, MNRAS, 430, 3017
Balogh, M. L., Navarro, J. F., & Morris, S. L. 2000, ApJ, 540, 113
Balogh, M. L., McGee, S. L., Wilman, D., et al. 2009, MNRAS, 398, 754
Bertin, E., & Arnouts, S. 1996, A&AS, 117, 393
Boselli, A., & Gavazzi, G. 2006, PASP, 118, 517
Bouy, H., Bertin, E., Barrado, D., et al. 2015, A&A, 575, A120
Butcher, H., & Oemler, Jr., A. 1978, ApJ, 219, 18
Capaccioli, M., & Schipani, P. 2011, The Messenger, 146, 2
Cava, A., Bettoni, D., Poggianti, B. M., et al. 2009, A&A, 495, 707
Couch, W. J., & Sharples, R. M. 1987, MNRAS, 229, 423
De Lucia, G., Boylan-Kolchin, M., Benson, A. J., Fontanot, F., & Monaco, P. 2010, MNRAS, 406, 1533
De Lucia, G., Weinmann, S., Poggianti, B. M., Aragón-Salamanca, A., & Zaritsky, D. 2012, MNRAS, 423, 1277
D'Onofrio, M., Bindoni, D., Fasano, G., et al. 2014, A&A, 572, A87
Dressler, A., Oemler, Jr., A., Couch, W. J., et al. 1997, ApJ, 490, 577
Ebeling, H., Voges, W., Bohringer, H., et al. 1996, MNRAS, 281, 799
Ebeling, H., Edge, A. C., Bohringer, H., et al. 1998, MNRAS, 301, 881
Ebeling, H., Edge, A. C., Allen, S. W., et al. 2000, MNRAS, 318, 333
Fasano, G., Marmo, C., Varela, J., et al. 2006, A&A, 445, 805
Fasano, G., Vanzella, E., Dressler, A., et al. 2012, MNRAS, 420, 926
Fritz, J., Poggianti, B. M., Cava, A., et al. 2011, A&A, 526, A45
Fritz, J., Poggianti, B. M., Cava, A., et al. 2014, A&A, 566, A32
Gunn, J. E., & Gott, III, J. R. 1972, ApJ, 176, 1
Haines, C. P., Merluzzi, P., Busarello, G., et al. 2011, MNRAS, 417, 2831
Jordi, K., Grebel, E. K., & Ammon, K. 2006, A&A, 460, 339
Kuijken, K. 2011, The Messenger, 146, 8
Larson, R. B., Tinsley, B. M., & Caldwell, C. N. 1980, ApJ, 237, 692
Lewis, I., Balogh, M., De Propris, R., et al. 2002, MNRAS, 334, 673
Mahajan, S., Mamon, G. A., & Raychaudhury, S. 2011, MNRAS, 416, 2882
Merluzzi, P., Mercurio, A., Haines, C. P., et al. 2010, MNRAS, 402, 753
Merluzzi, P., Busarello, G., Haines, C. P., et al. 2015, MNRAS, 446, 803
Mignano, A., Miralles, J.-M., da Costa, L., et al. 2007, A&A, 462, 553
Moran, S. M., Ellis, R. S., Treu, T., et al. 2007, ApJ, 671, 1503
Moretti, A., Poggianti, B. M., Fasano, G., et al. 2014, A&A, 564, A138
Omizzolo, A., Fasano, G., Reverte Paya, D., et al. 2014, A&A, 561, A111
Pimbblet, K. A., Smail, I., Kodama, T., et al. 2002, MNRAS, 331, 333
Poggianti, B. M., von der Linden, A., De Lucia, G., et al. 2006, ApJ, 642, 188
Poggianti, B. M., Calvi, R., Bindoni, D., et al. 2013, ApJ, 762, 77
Poggianti, B. M., Fasano, G., Omizzolo, A., et al. 2015, AJ, submitted [arXiv:1504.07105]
Ramella, M., Biviano, A., Pisani, A., et al. 2007, A&A, 470, 39
Retzlaff, J., Rosati, P., Dickinson, M., et al. 2010, A&A, 511, A50
Robotham, A. S. G., Norberg, P., Driver, S. P., et al. 2011, MNRAS, 416, 2640
Skrutskie, M. F., Cutri, R. M., Stiening, R., et al. 2006, AJ, 131, 1163
Smith, R. J., Lucey, J. R., Price, J., Hudson, M. J., & Phillipps, S. 2012, MNRAS, 419, 3167
Treu, T., Ellis, R. S., Kneib, J.-P., et al. 2003, ApJ, 591, 53
Valentinuzzi, T., Woods, D., Fasano, G., et al. 2009, A&A, 501, 851
Vandame, B. 2002, in SPIE Conf. Ser. 4847, eds. J.-L. Starck, & F. D. Murtagh, 123
Vandame, B. 2004, Ph.D. Thesis, Université de Nice
Varela, J., D'Onofrio, M., Marmo, C., et al. 2009, A&A, 497, 667
Vulcani, B., Poggianti, B. M., Aragón-Salamanca, A., et al. 2011, MNRAS, 412, 246
Wilman, D. J., Oemler, Jr., A., Mulchaey, J. S., et al. 2009, ApJ, 692, 298
York, D. G., Adelman, J., Anderson, Jr., J. E., et al. 2000, AJ, 120, 1579